

Emergent Structures in an Active Polar Fluid : dynamics of shape, scattering and merger

Kabir Husain and Madan Rao*

*Simons Centre for the Study of Living Machines, National Centre for
Biological Sciences (TIFR), Bellary Road, Bangalore 560 065, India*

(Dated: April 12, 2022)

Spatially localised defect structures emerge spontaneously in a hydrodynamic description of an active polar fluid comprising polar ‘actin’ filaments and ‘myosin’ motor proteins that (un)bind to filaments and exert active contractile stresses. These emergent defect structures are characterized by distinct textures and can be either static or mobile - we derive effective equations of motion for these ‘extended particles’ and analyse their shape, kinetics, interactions and scattering. Depending on the impact parameter and propulsion speed, these active defects undergo elastic scattering or merger. Our results are relevant for the dynamics of actomyosin-dense structures at the cell cortex, reconstituted actomyosin complexes and 2d active colloidal gels.

The dynamical interplay between defects, elasticity and flow has been a recurrent theme in the physics of condensed media [1]. This has been of particular interest in the context of active systems [2–7], where activity can give rise to spontaneous movement of defects, such as the rotation of spiral defects in active polar gels [8, 9], the translation of $+1/2$ disclinations in active nematics composed of filament-motor complexes [10] or the spontaneous formation of motile or static clusters of colloidal particles [4, 6, 7, 11]. The dynamics of defects and clusters and their influence on flows within the active medium have been the subject of many elegant experimental and theoretical studies [10, 12–14, 16–19, 21]. In many situations [15, 19, 20, 28], it is desirable to describe the emergent dynamics solely in terms of the coordinates and form factor of the emergent structures.

In this manuscript, we study the dynamics in two dimensions of polar filaments (‘actin’) actively driven by motor proteins (‘myosin’) that undergo turnover, i.e., binding/unbinding (with an estimated timescale of ~ 6 s *in vivo* [22]) [24, 29–31]. Recent studies on actomyosin-dependent molecular clustering at the cell surface and in *in-vitro* reconstitutions of a thin actomyosin layer on a supported membrane, provide our primary motivation [23–26]. Our main results are: (i) A variety of spatially compact defect structures, such as mobile virtual defects, rotating spiral defects or stationary asters, emerge spontaneously from an interplay between elastic, dissipative and active stresses. (ii) Activity drives defect motion and shape deformation, with isolated virtual defects moving as *extended particles*, dressed by a cloud of myosin density. (iii) These extended particles interact via the accompanying myosin cloud, and exhibit both *phoresis* and *taxis*. (iv) We study the dynamics, elastic scattering and (inelastic) merger of a pair of mobile defects as a function of impact parameter and self-propulsion velocity, by casting the effective dynamics in terms of defect coordinates and shape factor. We note that all the emergent characteristics of the extended particle - its integrity, dynamics and their mutual interactions, are consequences of the dressed myosin cloud.

Our results are obtained by solving hydrodynamic equations for a thin film of active fluid comprising actin filaments, described by a concentration c and orientation \mathbf{n} , and myosin motors, described by a filament-bound myosin

concentration ρ , which dissipate momentum via frictional damping at the cell substrate. The active contributions to the dynamics of c and \mathbf{n} come about *only in the presence of bound myosin* - the Supplementary contains a phenomenological derivation of the following simplified hydrodynamic equations, based on symmetry and conservation laws [9, 27],

$$\frac{\partial c}{\partial t} = -\vec{\nabla} \cdot \left(-D_a \vec{\nabla} c + v_0 c \mathbf{n} - W c \vec{\nabla} \rho \right) \quad (1)$$

$$\frac{\partial \rho}{\partial t} = -\vec{\nabla} \cdot \left(-D_m \vec{\nabla} \rho + v_0 \rho \mathbf{n} \right) + k_b \frac{c}{c + c_h} - k_u \rho \quad (2)$$

$$\begin{aligned} \frac{\partial \mathbf{n}}{\partial t} + \lambda(\rho)(\mathbf{n} \cdot \vec{\nabla}) \mathbf{n} &= K \nabla^2 \mathbf{n} - \zeta_0 \vec{\nabla} c + \zeta \vec{\nabla} \rho \\ &+ (\alpha(c) - \beta(c)n^2) \mathbf{n} \end{aligned} \quad (3)$$

where we have taken the active stress $\sigma^{act} = -W(c)\rho$ ($W < 0$, for contractility), and we work in the one-constant approximation [32]. We take $\alpha(c) = \nu(c/c_* - 1)$ and $\beta(c) = \nu(1 + c/c_*)$, which ensures that $|\mathbf{n}|^2 \rightarrow 1$ when $c \gg c_*$ [35]. In Eq. 3, $\zeta_0 > 0$ ensures positive filament compressibility, while $\zeta > 0$ describes the preferential alignment of the filament orientation to gradients of myosin density [31], here a consequence of the active stress.

We study the linear instability of the homogeneous, orientationally isotropic phase when $c_0 < c_*$, under the perturbations, $c(\mathbf{r}, t) = c_0 + \delta c(\mathbf{r}, t)$, $\rho(\mathbf{r}, t) = \rho_0 + \delta \rho(\mathbf{r}, t)$ and $\mathbf{n}(\mathbf{r}, t) = \delta \mathbf{n}(\mathbf{r}, t)$, where $\rho_0 = \frac{c_0}{c_0 + c_h} k_b / k_u$. We find two potential instability mechanisms: (i) the binding of myosin and the contractile advection of filaments ($\propto W c \vec{\nabla} \rho$) induces a density clumping instability when $k_b |W| \gtrsim D_a k_u$, with a band of unstable wavevectors between $k = 0$ and $k = \sqrt{|W| k_b c_0 - D_a k_u} / D_a$. Filament orientation remains disordered ($\langle \mathbf{n} \rangle = 0$). (ii) Myosin-induced torques ($\propto \zeta \vec{\nabla} \rho$) and self-advection ($\propto v_0 c \mathbf{n}$) drives a splay deformation ($|\vec{\nabla} \cdot \mathbf{n}| > 0$) and density clumping when $D_a |\alpha(c_0)| \lesssim v_0 \zeta \rho_0$, with a band of unstable wavevectors between $k = 0$ and $k = \sqrt{\frac{D_a k_u \alpha(c_0) + c_0 k_b v_0 \zeta}{D_a K k_u}}$. In both cases the instability towards clumping is non-oscillatory [33].

To see the fine structure of the emergent compact configurations, we need to go beyond the linear regime. We numerically integrate Eqs. 1-3 on a square grid with periodic boundary conditions using an explicit Forward-Time-Centred-Space (FTCS) scheme and appropriate initial con-

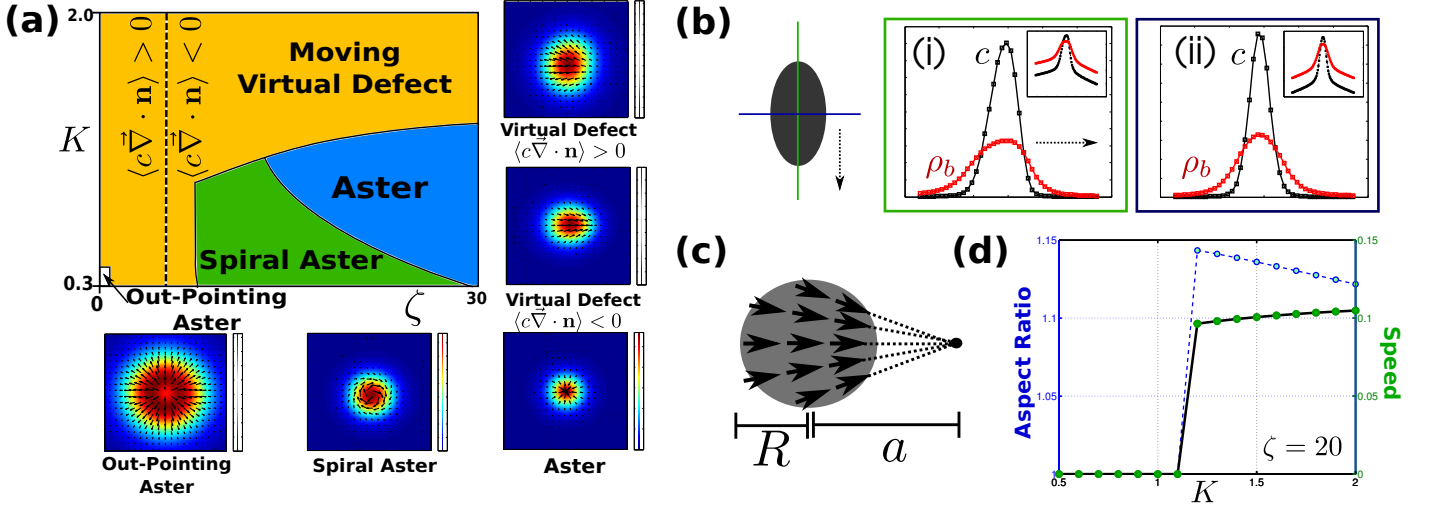


FIG. 1. (a) Typology of spatially compact single-defect structures in the $K - \zeta$ plane for a fixed concentration of filaments c_0 , together with snapshots of the textures formed by the filament orientation \mathbf{n} - the heat map represents c and the arrows represent $c\mathbf{n}$. All images are equally sized to show differences in size between the phases. (b) Myosin (red) and actin (black) concentration profiles within a moving virtual aster, along directions (i) longitudinal (green) and (ii) transverse (blue) to the direction of motion (dashed arrow). Insets show the same plotted on a semi-log scale to highlight the exponential tails. (c) Schematic of the *ansatz* used to describe the virtual aster - arrows represent the orientation \mathbf{n} , the dot represents the core of the virtual defect, and the grey circular domain represents the filament and myosin concentration. (d) Speed and aspect ratio of the clusters as a function of alignment strength K , obtained from the numerics and taken along the $\zeta = 20$ cut of the phase diagram in (a). Here $v_0 = 0.1$.

ditions [33]. Starting from a homogeneous, isotropic phase, we observe that the system quickly settles down to an evolving population of spatially compact actin-myosin clusters (Movies 1, 2 [33]). To explore the typology of compact structures formed, we choose initial conditions that produce a single defect, spanning K and ζ (Fig. 1(a)).

Figure 1(a)-(d) shows the single-defect phase diagram together with the compact density profiles and orientation textures that obtain. All structures consist of a compact accumulation of actin filaments dressed by a wider myosin cloud (Fig. 1(b)). At low K they are radially symmetric with zero net polarity ($\langle c\mathbf{n} \rangle = 0$) and hence static. The orientation texture is set by the control parameter ζ/ζ_0 . When ζ/ζ_0 is small (large) the term $\zeta_0 \vec{\nabla} c$ ($\zeta \vec{\nabla} \rho$) dominates to form an out(in)-pointing aster. As we show in the SI, integrating out the myosin density when it is ‘fast’, in the limit of large ζ/ζ_0 , results in effective equations for the active filament identical to those analyzed in [24, 34], with an effective ‘negative compressibility’ in the \mathbf{n} -equation [35]. At an intermediate value of ζ/ζ_0 , $\zeta_0 \vec{\nabla} c$ dominates at the core of the domain and $\zeta \vec{\nabla} \rho$ dominates at the boundary, forming a spiral aster texture, which rotates with an angular velocity $\omega(r) \propto v_0 n_\theta(r)$ [8, 9].

When K is large the defect core moves abruptly from within to outside the compact domain, giving rise to a *apparent* or *virtual defect* (Fig. 1(c)) [36–38]. Depending on the relative strength of $\zeta \vec{\nabla} \rho$ and $\zeta_0 \vec{\nabla} c$, the virtual defect is either a virtual out-pointing-aster ($\langle c\vec{\nabla} \cdot \mathbf{n} \rangle > 0$) or a virtual aster ($\langle c\vec{\nabla} \cdot \mathbf{n} \rangle < 0$).

These textures can be qualitatively understood as arising from a competition between the first three terms on the R.H.S. of Eq. 3. We may analyse this further by not-

ing that the dynamics of \mathbf{n} (when $\lambda = 0$) can be obtained as $\partial_t \mathbf{n} = -\delta \mathcal{L} / \delta \mathbf{n}$, where the Lyapunov function $\mathcal{L} = \int d^2x \left[K (\partial_i n_j) (\partial_i n_j) + (\zeta \rho - \zeta_0 c) \vec{\nabla} \cdot \mathbf{n} \right]$. The quantity $\zeta \rho - \zeta_0 c$ thus promotes a spontaneous splay [38, 39], with a negative (positive) divergence when $\zeta \rho - \zeta_0 c > 0$ (< 0). The Lyapunov function \mathcal{L} is analogous to the free energy of textured Langmuir domains [36, 38], indicating that the transition between aster and virtual defect is first order, as a function of the control parameter $R_a(\zeta \rho_0 - \zeta_0 c_0)/K$ [36].

The profile of filament and myosin densities is set by the interplay between the binding and advective nonlinearities and is difficult to obtain an exact expression. However, we may exploit the compactness of the filament domain, which implies that $c(\mathbf{r}) \approx 0$ and $|\mathbf{n}| \approx 0$ for $r > R_a$ (where R_a is some distance from the centre of the domain, naturally interpreted as the radius of the filament domain), to analyse the decay of the dressed cloud of myosin. The outer solution (i.e., for $r > R_a$) for ρ at steady state is given by the balance between diffusion and unbinding: $D_m \nabla^2 \rho = k_u \rho$. The radially symmetric solution is found to be,

$$\rho(r) = A_1 K_0(r/r_0) \quad (4)$$

where $K_\nu(r)$ is the modified Bessel function of the second kind and the length scale $r_0 = \sqrt{D_m/k_u}$. The constant A_1 may be determined by matching the inner solution ($r < R_a$, where $|\mathbf{n}|$ and $c \geq 0$) with the outer solution at the boundary $r = R_a$.

The sudden appearance of a net polarity ($|\langle c\mathbf{n} \rangle| > 0$) manifests as a shape distortion away from circularity and a centre-of-mass motion driven by the self-advection current, $\propto c\mathbf{n}$, which we analyse to lowest order in deformation. We

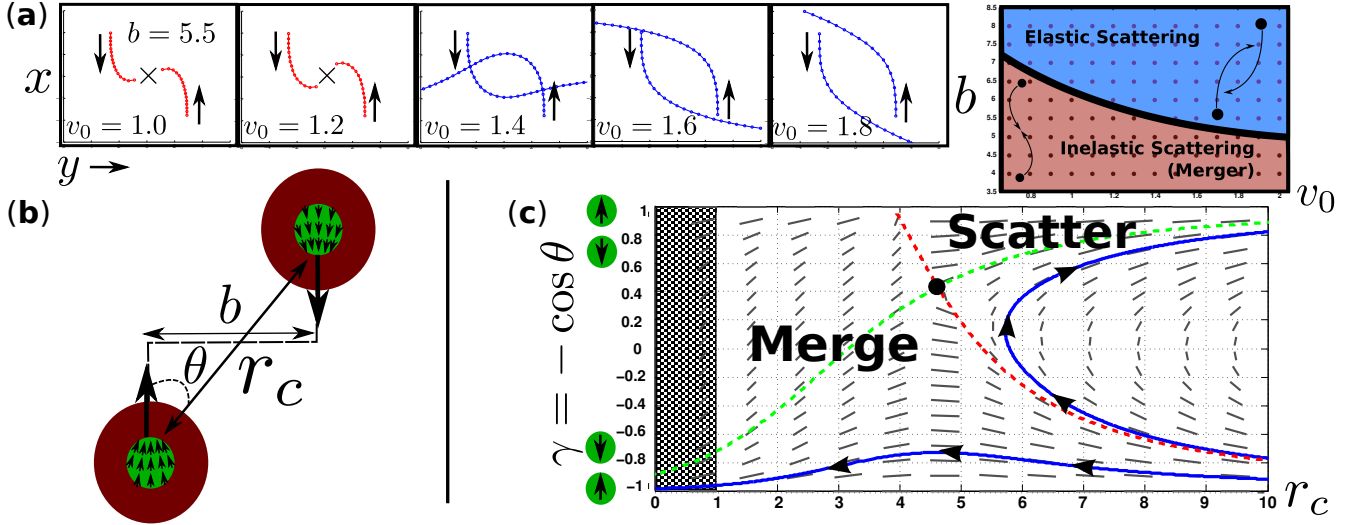


FIG. 2. (a) Left - several representative trajectories from the numerics with varying v_0 and fixed $b = 5.5$. Right - The outcome of the numerical integration as a function of impact parameter b and self-advection v_0 . Blue represents scattering and escape, Red represents merger (depicted as a \times). (b) Left - The scattering geometry, where green represents the filament density and the arrows the filament orientation. The red represents the bound myosin density. (c) The phase portrait of the scattering dynamical system, Eqs. 9, generated using the software *pplane* (<http://math.rice.edu/~dfield/dfpp.html>). The black dot is the saddle point whose unstable separatrix (red dashed line) separates the merge region from the scattering region. Plotted in green is the stable separatrix to which individual trajectories converge. In blue are two example trajectories. Gray lines show the flows of the dynamical system. The shaded region is the distance at which the merger will occur.

transform to a comoving frame with velocity \mathbf{v}_c , which for $r > R_a$ gives $D_m \nabla^2 \rho + \mathbf{v}_c \cdot \nabla \rho = k_u \rho$, and expand in circular modes $\rho(r, \theta) = \sum \rho_m(r) e^{im\theta}$. We solve for the lowest order axisymmetric steady-state solution: i.e. of the form $\rho_0(r) + \rho_1(r) \cos \theta$, where $\theta = 0$ is the direction of motion. When deviations from circularity are small ($\rho_1 \ll \rho_0$), ρ_0 is given by Eq. 4 and

$$\rho_1(r) = A_2 K_1 \left(\frac{r}{r_0} \right) - \frac{v_c}{\sqrt{D_m k_u}} A_1 r K_0 \left(\frac{r}{r_0} \right) \quad (5)$$

where A_2 may once again be obtained from matching the inner and outer solutions at $r = R_a$.

Higher order contributions to the shape of the filament and myosin domains arise from both motion and the texture of the domain. In the numerics we observe elliptic deformations stretching the cluster in (perpendicular to) the direction of motion when $\langle c \vec{\nabla} \cdot \mathbf{n} \rangle < 0$ ($\langle c \vec{\nabla} \cdot \mathbf{n} \rangle > 0$). This may be attributed to the non-vanishing component of \mathbf{n} transverse to the direction of motion. Concurrent with this, we find that as the extent of splay in the orientation field reduces (i.e., as K increases), so does the ellipticity (Fig. 1(d)).

From our numerical analysis, we find that an isolated moving virtual defect with its myosin cloud maintains its shape and texture over time. The density and orientation fields then obey a traveling front form $c = c(\mathbf{r} - \mathbf{R}(t))$, $\mathbf{n} = \mathbf{n}(\mathbf{r} - \mathbf{R}(t))$, $\rho = \rho(\mathbf{r} - \mathbf{R}(t))$, where $\mathbf{R}(t)$ is the centre-of-mass of the filament domain. We may thus describe the motion of a single virtual defect, isolated from others, solely in terms of its centre-of-mass coordinate $\mathbf{R}(t) \equiv c_t^{-1} \int_{\Omega} d^2 r \mathbf{r} c$ and net polarity $\mathbf{p}(t) \equiv c_t^{-1} \int_{\Omega} d^2 r \mathbf{n} c$, where $c_t = \int_{\Omega} d^2 r c$,

where Ω is the compact support of the defect,

$$\begin{aligned} \dot{\mathbf{R}}(t) &= \frac{1}{c_t} \int d^2 r \mathbf{J}_f \approx \frac{v_0}{c_t} \int d^2 r c \mathbf{n} = v_c \hat{\mathbf{p}}(t) \\ \dot{\mathbf{p}}(t) &= \frac{1}{c_t} \int d^2 r c \underbrace{\left(\frac{\mathbf{J}_f}{c} \cdot \vec{\nabla} + \frac{\partial}{\partial t} \right)}_{\text{convective derivative}} \mathbf{n} = 0 \end{aligned} \quad (6)$$

where the overdot is a time derivative. Above, we have made use of the fact that filament diffusion $D_a \vec{\nabla} c$ and the $Wc \vec{\nabla} \rho$ term are responsible for maintaining the size of the moving domain, and hence they balance to 0 everywhere. This leaves only the contribution from self-advection ($\propto v_0 c \mathbf{n}$) in the first equation.

The speed of the domain, $v_c = v_0 |\mathbf{n}^c|$, may be approximately calculated from the *ansatz* shown in Fig. 1(c) and is found to increase from $\sim 0.85v_0$ to v_0 as the defect core moves further from the centre of the domain. This is consistent with the numerics (Fig. 1(d)), though we note that the asymmetric profile of the filament and myosin fields will also contribute to the speed of the domain. *The isolated moving defect thus behaves as an extended particle with inertia, with a well defined mass and momentum.*

We next investigate the interaction between these particles mediated by the myosin field - stationary defects do not interact unless they are close enough to allow for a finite overlap between their myosin clouds, with a interaction length scale $r_0 = \sqrt{D_m/k_u}$ - this interaction leads to their merger (Movie 1 [33]). On the other hand, moving virtual defects may initially be well separated and then approach each other (Movie 2 [33]). Here we investigate the interplay between their self-propulsion and the myosin mediated dynamical interaction. We derive interactions between virtual

defects by decomposing the microscopic fields into their contributions from the each domain ($c = \sum c_i$, etc.), valid when the domains are well separated ($|\mathbf{R}_i - \mathbf{R}_j| > R_a$, the size of each domain), and define the centre of mass and polarity of the each cluster (\mathbf{R}_i and \mathbf{p}_i) as before. Using the shorthand $\mathbf{R}_{ij} = \mathbf{R}_i - \mathbf{R}_j$,

$$\begin{aligned}\dot{\mathbf{R}}_i(t) &= v_c \mathbf{p}_i(t) - \sum_{j \neq i} \frac{W}{c_t^{(i)}} \int d^2r c_i(\mathbf{r}) \vec{\nabla} \rho_j(\mathbf{r} + \mathbf{R}_{ij}) \\ \dot{\mathbf{p}}_i(t) &= \sum_{j \neq i} \frac{\zeta}{c_t^{(i)}} \int d^2r c_i(\mathbf{r}) \vec{\nabla} \rho_j(\mathbf{r} + \mathbf{R}_{ij})\end{aligned}\quad (7)$$

The second equation must be augmented with the constraint that the magnitude of each \mathbf{p}_i is constant.

We develop the integral appearing in both equations into a multipole expansion, valid when the length scale over which the myosin cloud varies, r_0 , is larger than the characteristic size of the virtual defect. Writing $\rho_j(\mathbf{r} + \mathbf{R}_{ij}) = \rho_j(\mathbf{R}_{ij}) + \mathbf{r} \cdot \vec{\nabla}' \rho_j(\mathbf{R}_{ij}) + \mathcal{O}(r^2)$, where $\mathbf{R}_{ij} = \mathbf{R}_i - \mathbf{R}_j$ and the prime indicates the derivative with respect to \mathbf{R}_{ij} , and expanding $c_i(\mathbf{r})$ to first order in axisymmetric circular harmonics, $c_i(\mathbf{r}) = c_i^{(0)} + c_i^{(1)} \frac{\mathbf{p}_i \cdot \mathbf{r}}{r} + \dots$,

$$\begin{aligned}\int d^2r c_i(\mathbf{r}) \vec{\nabla} \rho_j(\mathbf{r} + \mathbf{R}_{ij}) &\approx \left[2\pi \int dr r c_i^{(0)} \right] \nabla' \rho_j(\mathbf{R}_{ij}) \\ &+ \left[\pi \int dr r^2 c_i^{(1)} \right] \mathbf{p}_i \cdot \nabla' \nabla' \rho_j(\mathbf{R}_{ij}) \\ &+ \text{quadrupolar and higher terms}\end{aligned}\quad (8)$$

The expressions in square brackets correspond to the monopole and dipole moments of the filament density. Expanding now the myosin field into axisymmetric circular harmonics $\rho(\mathbf{R}) = \rho^{(0)}(R) + \rho^{(1)}(R) \frac{\mathbf{p} \cdot \mathbf{R}}{R} + \dots$ and using the forms given in Eqs. 4, 5, we obtain after a straightforward calculation the effective equations of motion for a population of interacting virtual defects. Note that, as each ρ_j decays away from R_j , the signs of W and ζ give rise to an attractive ‘force’ (*taxis*) and an attractive ‘torque’ (*phoresis*), respectively, between virtual defects [20, 40].

We now turn to the consequences of Eqs. 7 and 8 on the ‘scattering’ of virtual defects. First, we investigate this in the geometry depicted in Fig. 2(b) by numerically integrating the full equations of motion, Eqs. 1-3. Figure 2(a) shows that for large impact parameter b or for large self-propulsion speed v_0 the two clusters ‘elastically scatter’ off each other and escape to the far field (Movie 3 [33]), whereas for low b or low v_0 they merge (Movie 4 [33]). Interestingly, as seen in the trajectories shown in Fig. 2(a), the deflection angle of scattering decreases with v_0 even for a fixed b . This is reminiscent of the scattering of inertial particles, even though the ‘extended particles’ here are formed by constituents undergoing overdamped dynamics.

The symmetry of the scattering geometry of Fig. 2(b) can be exploited to develop an analytic representation of the scattering process. We define the following variables: the distance of one virtual defect from the other, $r_c = |\mathbf{R}_{21}|$, and the radial projection of the polarity vector, $\gamma = \mathbf{R}_{12} \cdot \mathbf{p}_1 / r_c$. Using Eqs. 7, 8 and retaining for simplicity only the

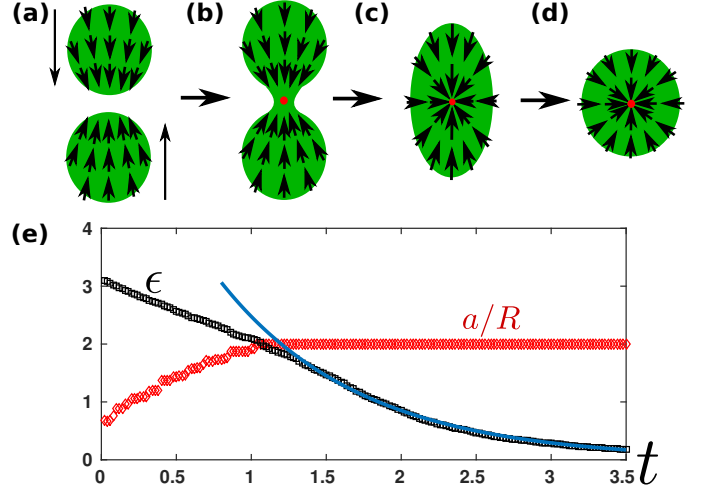


FIG. 3. A schematic of the sequence of events in merger, namely (a) approach of the clusters, mediated by the myosin clouds, followed by (b) filament overlap and neck formation, which (c) grows to form an elliptic domain that (d) relaxes exponentially to a radially symmetric domain. (e) Time evolution of the ratio of the neck width a to the single domain radius R (red diamonds) as well as the shape factor $\epsilon = d_{\text{maj}}/d_{\text{min}} - 1$ (black squares), where d_{maj} , d_{min} are the lengths of the major and minor axes of the ellipse enclosing the merging domain area. The blue line is an exponential fit.

radially symmetric terms in c and ρ (i.e., Eq. 4 and the monopole term in Eq. 8), gives the ODE’s,

$$\begin{aligned}\dot{r}_c &= 2v_c \gamma + 2\bar{W} K_1 \left(\frac{r_c}{r_0} \right) \\ \dot{\gamma} &= (1 - \gamma^2) \left(2\frac{v_c}{r_c} - \bar{\zeta} K_1 \left(\frac{r_c}{r_0} \right) \right)\end{aligned}\quad (9)$$

where $\bar{W} = WA_1/r_0$ and $\bar{\zeta} = \zeta A_1/r_0$.

A representative phase portrait of this dynamical system is depicted in Fig. 2(c). When $2v_c > \bar{\zeta} r_0$ there exists a single fixed point, a saddle node at $\gamma = 1$ and r_c is the solution of $-\bar{W} K_1(r_c/r_0) = v_c$. When $2v_c < \bar{\zeta} r_0$, the dynamical system has two fixed points (r_1^*, γ_1^*) and (r_2^*, γ_2^*) . (r_1^*, γ_1^*) is the one described above, while (r_2^*, γ_2^*) is the solution of $2v_c = \bar{\zeta} r_2^* K_1(r_2^*/r_0)$ and $\gamma_2^* = -2\bar{W}/\bar{\zeta} r_2^*$. When $\gamma_2^* > 1$, the first fixed point is a saddle node and the second a nodal source [41]. Conversely, when $\gamma_2^* < 1$ (as depicted in Fig. 2(c)) the first is a nodal source and the second a saddle node. Importantly, the system has only a single saddle node, which is always between $0 < \gamma \leq 1$. Thus, in the physically relevant region of the phase plane $-1 < \gamma < 1$, the unstable separatrix of this saddle node acts as a phase boundary between merger and elastic scattering.

Note, in particular, that all trajectories escape to infinity or end in a merging - there exist no bound states.

We end with a brief discussion on the sequence of events that occur when two domains merge. We find numerically that when two clusters merge in a head-on collision they do so in the following stereotypic manner (Fig. 3(a) and Movie 6 [33]) - (i) initial overlap of the concentration fields

leads to the formation of a neck region, which develops an aster defect (ii) the neck widens to produce an elliptic domain which then (iii) relaxes exponentially to a radially symmetric domain with an aster defect, Fig. 3(b).

We numerically investigate the further fate of the merged domain. When K is large the aster core is unstable [36] and moves out of the merged domain. Conversely, when K is small, the defect core is stable and remains to form a stationary aster or spiral aster (contrast Movies 4 and 5 [33]). In the intermediate regime, we find that the fate of the domain depends on the impact parameter b and the self-advection speed v_0 , revealing the dynamical nature of the interacting myosin field. We will carry out a detailed study of the dynamics of merger in a later work.

In summary, we have conducted a detailed study of the form and dynamics of the compact, emergent structures that arise in a hydrodynamic description of an active polar fluid with associated ‘motor’ elements. By explicit construction of effective equations of motion, we have demonstrated that these structures behave as extended self-propelled particles that exhibit both phoresis and taxis. We expect our results to be relevant to systems exhibiting both self-propulsion as well as contractile stresses, such as might be expected for the dynamics of actomyosin structures as the cell surface [24]. We look forward to experimental tests of our predictions in *in vivo* as well as *in vitro* contexts [42].

We thank Sriram Ramaswamy, K. VijayKumar, Amit Kumar Singh, B. R. Ujwal and the members of the Simons Centre for the Study of Living Machines for insightful and enjoyable discussions.

* madan@ncbs.res.in; on lien from *Raman Research Institute, C.V. Raman Avenue, Bangalore 560080, India*

- [1] P.M. Chaikin and T.C. Lubensky. *Principles of Condensed Matter Physics*. Cambridge University Press, 2000.
- [2] Giomi et. al., Phys. Rev. Lett. **106** 218101 (2011).
- [3] Giomi et. al., Phys. Rev. Lett. **101** 198101 (2008).
- [4] Buttioni et. al., Phys. Rev. Lett. **110** 238301 (2013).
- [5] A. Menzel, T. Ohta and H. Lowen. Phys. Rev. E **89** 022301 (2014).
- [6] Palacci et. al., Science, 22 February 2013.
- [7] Theurkoff et. al., Phys. Rev. Lett. **108**, 268303 (2012).
- [8] K. Kruse, J. F. Joanny, F. Julicher, J. Prost, and K. Sekimoto, Phys. Rev. Lett. **92**, 078101 (2004).
- [9] M.C. Marchetti et al., Rev. Mod. Phys. **85**, 1143 (2013).
- [10] Sanchez et. al., Nature **491**, 431434 (2012).
- [11] O. Powl and H. Lowen. Phys. Rev. Lett. **112** 238303 (2014).
- [12] E. Putzig, GS Redner, A Baskaran, A Baskaran. Soft Matter (2016).
- [13] L. M. Pismen. Phys. Rev. E **88**, 050502 (2013).
- [14] Giomi et. al., Phil. Trans. R. Soc. A (372) 20130365 (2014).
- [15] Giomo et. al. Phys. Rev. Lett. **110**, 228101 (2013).
- [16] Doostmohammadi et. el., Nature Comm., **7**, 10557 (2016).
- [17] M. Neef and K. Kruse. Phys. Rev. E **90**, 052703 (2014).
- [18] A. Kaiser and H. Lowen. Phys. Rev. E **87**, 032712 (2013).
- [19] Keber et. al., Science, 5 September 2014.
- [20] S. Yabunaka and N. Yoshinaga. arXiv preprint arXiv:1604.00593 (2016).
- [21] DeCamp et. al., Nature Materials **32** 1 (2015).
- [22] M. Fritzsche, A. Lewalle, T. Duke, K. Kruse, G. Charras. Mol. Biol. Cell, **24**, 757-767 (2013).
- [23] D. Goswami et. al., Cell **135**, 1085 (2008).
- [24] K. Gowrishankar, S. Ghosh, S. Saha, C. Rumamol, S. Mayor and M. Rao, Cell **149**, 1353 (2012).
- [25] R. Raghupathy et. al., Cell **161**, 581 (2015).
- [26] A. Das, A. Polley, and M. Rao. Phys. Rev. Lett. **116**, 068306 (2016).
- [27] J. Toner and Y. Tu, Phys. Rev. Lett. **75**, 4326 (1995).
- [28] M. Hagan and A. Baskaran. arXiv:1602.03388 (2016).
- [29] Ahmadi, A. and Liverpool, T. B. and Marchetti, M. C.. Phys. Rev. E **74** 061913 (2006).
- [30] H. Y. Lee and M. Kardar. Phys. Rev. E **64**, 056113 (2001).
- [31] S. Sankararaman, G. I. Menon, and P. B. Sunil Kumar. Phys. Rev. E **70**, 031905 (2004).
- [32] P-G. de Gennes, J. Prost. *The Physics of Liquid Crystals* Clarendon Press, 1993
- [33] See Supplemental Material at [URL will be inserted by publisher] for numerical details, details of the analytical calculations and Movies.
- [34] K. Gowrishankar and M. Rao, Soft Matter **12**, 2040 (2016).
- [35] A. Gopinath, M. F. Hagan, M. C. Marchetti, and A. Baskaran. Phys. Rev. E **85**, 061903 (2012).
- [36] D. Pettey and T. C. Lubensky. Phys. Rev. E **59**, 1834 (1999).
- [37] S.A. Langer and J.P. Sethna, Phys. Rev. A **34**, 5035 (1986).
- [38] R.C. Sarasij and M. Rao, Phys. Rev. Lett. **88**, 088101 (2002); R. C. Sarasij, P. Srivastava, and M. Rao. Phys. Rev. E **85**, 041920 (2012).
- [39] P. Srivastava, R. Shlomovitz, N. S. Gov, and M. Rao. Phys. Rev. Lett. **110**, 168104 (2013).
- [40] S. Saha, R. Golestanian, and S. Ramaswamy. Phys. Rev. E **89**, 062316 (2014).
- [41] S. Strogatz. *Nonlinear Dynamics and Chaos*, Levant Books, Calcutta, 2007.
- [42] D. Koester et. al., PNAS **113**, 1645-1654 (2016).